PAPER • OPEN ACCESS

Material jetting of carbon nano onions for printed electronics

View the article online for updates and enhancements.

Material jetting of carbon nano onions for printed electronics

Rui M R Pinto[1] , **Siva Sankar Nemala**[1] , **Mohammadmahdi Faraji**[1] ,
Joao Fernandes[1], **Clara Ponte**[1], **Giovanni De Bellis**[2,3] , **Aritz Retolaza**[1] ,
K B Vinayakumar[1,*] **and Andrea Capasso**[1,*]

[1] International Iberian Nanotechnology Laboratory, Braga, Portugal
[2] Department of Astronautical, Electrical and Energy Engineering, Sapienza University of Rome, Rome, Italy
[3] Research Center on Nanotechnology Applied to Engineering of Sapienza (CNIS), Sapienza University of Rome, Rome, Italy

E-mail: vinaya.basavarajappa@inl.int and andrea.capasso@inl.int

CrossMark

Abstract

As an additive manufacturing process, material jetting techniques allow to selectively deposit droplets of materials in liquid or powder form through a small-diameter aperture, such as a nozzle of a print head. For the fabrication of printed electronics, a variety of inks and dispersions of functional materials can be deposited by drop-on-demand printing on rigid and flexible substrates. In this work, zero-dimensional multi-layer shell-structured fullerene material, also known as carbon nano-onion (CNO) or onion-like carbon, is printed on polyethylene terephthalate substrates using drop-on-demand inkjet printing. CNOs are produced using a low-cost flame synthesis technique and characterized by electron microscopy, Raman, x-ray photoelectron spectroscopy, and specific surface area and pore size measurements. The produced CNO material has an average diameter of $\sim$33 nm, pore diameter in the range $\sim$2–40 nm and a specific surface area of 160 m^2.g^{-1}. The CNO dispersions in ethanol have a reduced viscosity ($\sim$1.2 mPa.s) and are compatible with commercial piezoelectric inkjet heads. The jetting parameters are optimized to avoid satellite drops and to obtain a reduced drop volume (52 pL), resulting in optimal resolution (220 μm) and line continuity. A multi-step process is implemented without inter-layer curing and a fine control over the CNO layer thickness is achieved ($\sim$180 nm thick layer after 10 printing passes). The printed CNO structures show an electrical resistivity of $\sim$600 Ω.m, a high negative temperature coefficient of resistance (-4.35×10^{-2} $^\circ$C^{-1}) and a marked dependency on relative humidity (-1.29×10^{-2} RH$_\%^{-1}$). The high sensitivity to temperature and humidity, combined to the large specific area of the CNOs, make this material and the corresponding ink a viable prospect for inkjet-printed technologies, such as environmental and gas sensors.

Supplementary material for this article is available online

Keywords: drop-on-demand printing, nanomaterials, negative temperature coefficient of resistivity, humidity dependency, sensors

(Some figures may appear in colour only in the online journal)

---

* Authors to whom any correspondence should be addressed.

1. Introduction

While conventional electronics relies on micro- and nano-fabrication processes (e.g. thin film deposition, photolithography, etching, etc), flexible electronics underpins on additive

manufacturing techniques, such as blade-coating, slot-die coating, screen printing, gravure printing, offset printing, nanoimprinting, flexography, spray coating and inkjet printing (IJP) [1]. Drop-on-demand IJP is a low-cost, low-energy alternative to photolithography-based processes, as it allows the deposition of ink/solution drops in predetermined positions for the fabrication of $10–100\,\mu$m scale electronic devices, while reducing material consumption [2]. A vast, comprehensive assortment of printable inks needs to be available to print the various components of numberless electronic devices. Many materials and composites have been developed and optimized to this end, tailoring their properties to the specific requirements of each component. For the printing of contacts and interconnect lines, metal- and metal oxide-containing inks are the most common choices. Metal nanoparticle (NP) inks (e.g. Au, Ag and Cu) are commercially available and have curing temperatures of $\sim$120 °C–150 °C, compatible with many polymer substrates. Aqueous-based commercial inks compatible with IJP have viscosities in the range 3–12 mPa.s, the surface tension is typically $\sim$19–35 mN.m^{-1} and contain particles with diameters of $\sim$10–100 nm. Structures printed with aqueous-based silver nanoparticle (Ag-NP) ink exhibit a volume resistivity of the order of 10^{-2}–10^{-4} Ω.m for curing temperatures in the range 100 °C–250 °C [3, 4]. Materials with negative temperature coefficient of resistance (NTCR) undergo a decrease in resistance proportional to a temperature increase. As opposed to solid, crystalline metals, this behavior is observed in ceramic or polymeric thermistors, Ni–Cr alloys, some metal oxides, Si and Ge, and carbon-based materials (CBM) [5–8]. NTCR materials are used in temperature compensation applications (e.g. voltage references, oscillators, amplifiers, and high-frequency transistors) and are particularly suited to fabricate accurate temperature and humidity sensors. CBMs in particular can be proficiently used for the IJP fabrication of these devices. To date, the IJP of CBMs has been demonstrated for graphene [9, 10], carbon nanotubes [11], C_{60} fullerenes [12] and [6,6]-phenyl C_{61} butyric acid methyl ester fullerene blends [13]. A variety of other two-dimensional materials have been inkjet-printed too [14–18]. Carbon-based, printable inks also exist in the market, for example in the form of carbon black NP inks (water-based), which have resistivity of 50–80 Ω.m [19]. The IJP of multi-layer shell-structured fullerene material, also known as carbon nano-onion (CNO) or onion-like carbon (OLC) has been first reported in 2022 [20].

In 1992, Ugarte *et al* originally reported the production of CNOs by the electron beam irradiation of carbon precursors [21]. Due to the irradiation, the material reorganized into quasi-spherical structures comprised of concentric graphitic shells as large as 47 nm ($\sim$70 shells), where the distance between layers was 3.34 Å, close to that of bulk graphite. In previous reports, CNOs have been prepared by a number of techniques, where the most common are nano-diamond annealing, resulting in small CNOs with 6–8 shells (5 nm), and arc discharge, for the preparation of large CNOs with 20–30 shells (15–25 nm) [22]. The reported density of CNOs (with diameter in the range 4–36 nm) is $\sim$1.64 g.cm^{-3}, lower than that of graphite (2.25 g.cm^{-3}) [23]. In terms of applications, CNOs have been utilized as lubricants, in optical limiting, in catalysis, in medicine (e.g. as biological markers and biosensors), in environmental remediation, in electronics (e.g. as capacitor and battery electrodes, and for shielding applications) [24–27].

In this paper, CNOs with marked NTCR produced by a low-cost method are used to prepare low-viscosity, IJP-compatible dispersions that can be ejected by drop-on-demand piezoelectric inkjet heads. The ink is prepared in ethanol, which allows for fast room-temperature evaporation of the solvent and the printing of μm-thick structures without the need for curing between layers. Following CNO material and ink characterization, the jetting and printing parameters are optimized. Lastly, electrical characterization of the printed devices is performed and the environmental sensitivity of the materials is studied. For comparison purposes, a commercial water-based Ag-NP ink was subjected to the same tests. Overall, this work details the IJP process of CNO-based inks, while exploring the electrical properties of the prints and their sensitivity against temperature and humidity changes.

2. Experimental section

2.1. CNO Ink preparation and characterization

CNOs were prepared by a flame synthesis technique, as previously reported and illustrated in figure S1 [20]. For transmission electron microscopy measurements (TEM, JEOL 2100, operated at 200 kV), 20 μL of the dispersion were drop-cast on a Cu grid (lacey carbon, 200 mesh) and dried at 60 °C for 15 min. Raman analysis was carried out with an ALPHA300 R Confocal Raman Microscope (WITec), using 532 nm laser light for excitation, at room temperature. Single acquisitions were performed using a 600 grooves mm^{-1} grating with 2 mW of laser power. X-Ray photoelectron spectroscopy (XPS) measurements were done with an ESCALAB 250 Xi system in ultra-high vacuum conditions. Nitrogen (N_2) adsorption/desorption isotherms were performed at 77 K using a Quantachrome Autosorb IQ2 automated analyzer. Prior to the measurements, the samples were outgassed under vacuum at 350 °C for 3 h (heating rate of 5 °C min^{-1}). The surface area (S_{BET}) was calculated by the Brunauer–Emmett–Teller (BET) method using ASIQwin™ software ($P/P_0 = 0.025$–0.3, $R^2 = 0.9986$, C constant $= 30.66$) [28]. Pore size distribution was assessed using the Barett–Joyner–Halenda (BJH) method of the desorption branch [29]. The total specific pore volume was determined from the total amount of N_2 adsorbed at relative pressure $P/P_0 = 0.95$. The purified CNO was mixed in ethanol (6 mg ml^{-1}), and ultra-sonicated (30 min) to achieve homogeneity (remained stable for several weeks). The rheological behavior of CNO-based inks was assessed through steady flow rotational measurements, carried out on an Anton Paar MCR 302 rotational rheometer, equipped with a double gap measuring system, suitable for low viscosity samples.

2.2. Inkjet-printing of functional inks

The IJP of the two inks under study was achieved with a piezoelectric inkjet head (Pico-Tip J, by GeSiM mbH, Germany) containing a single nozzle (25 μm diameter). For printing, the head was scanned across the substrate using precision motors and stages (Thorlabs, Inc.). The driving waveform was composed of two square pulses of opposite polarity, with lengths Δt_1 (amplitude V_-) and Δt_2 (amplitudes V_+). The rise and fall times (t_{rise}) are ∼1 μs. The backpressure of the ink in the inkjet head was controlled by leveling the reservoir (open to atmospheric pressure) above or below the nozzle opening (meniscus). The nozzle-substrate distance (throw distance) was 1.5 mm. For droplet observation, a drop-watching system comprised of a microscope and a light-emitting diode (LED) backlight was used. The schematic representation of the drop-watching setup and the printing setup are provided in figures S2(a) and (b), respectively. An example of piezoelectric actuation timing and LED actuation with three pulses is given in figure S2(c). An optical micrograph of inkjet drops at three distinct time points after ejection is shown in figure S2(d). The printing tests were performed on 75 μm thick flexible polyethylene terephthalate (PET) sheets (Hostaphan® GN CT01B, Mitsubishi Polyester Film GmbH), which are provided by the manufacturer with a double-sided coating to improve ink adhesion. After printing, the inks were completely cured by heating the substrates at 120 °C for 60 min (Ag-NP ink), or 5 min (CNO ink), on a hotplate.

Static contact angle measurements were carried out on the same type of PET substrates, using a drop shape analysis system (DSA−100, Krüss GmbH). The contact angles of deionized (DI) water, ethanol, Ag-NP ink and CNO ink drops were measured (in triplicate, for each liquid) at a controlled temperature (21 °C) and relative humidity of 45%. The substrate was placed on the measurement platform and a 5 μL droplet of the corresponding liquid was deposited on the surface using a micropipette. The images of the droplets were recorded immediately (especially important in the ethanol measurements, which evaporate in a matter of seconds). The contact angles were calculated using an elliptical fit ('Contact Angle' plug-in, running on ImageJ [30]). After printing, the test structures were studied by optical microscopy, stylus profilometry (Tencor™ P-16 Surface Profiler, KLA Corporation) and scanning electron microscopy (SEM) (FEI Nova NanoSEM 650). To obtain detailed topography images of the printed test structures, SEM was performed at low acceleration voltages (3.0 kV) and with a 15° substrate tilt. For the comparison of the printing resolution and electrical properties, a commercial Ag-NP ink (Metalon® JS-A221AE, Novacentrix Corp.) was subjected to the same tests as the CNO ink. To illustrate the typical drop size, drop velocity and actuation conditions, deionized water and a glycerol solution with known viscosity were also jetted in the drop optimization study. All solutions were filtered (5 μm) to remove dust particles and solid contaminants prior to loading them into the inkjet head.

2.3. Electrical measurements

To measure the conductivity of the inkjet-printed materials, 2 cm long traces were printed using 2-pass printing and 50-pass printing for the Ag-NP and CNO inks, respectively. The cross-sectional area of the traces was 78.5 μm^2 for the Ag-NP trace and 124.89 μm^2 for the CNO trace. Pads were manually deposited at the end of the test traces (nickel conductive paste, CW2000, ITW Chemtronics, USA) and then 4-point probe measurements of the resistivity (at 25 °C) were performed with a source measure unit (Keithley 2410 Sourcemeter). The temperature coefficient of resistance (TCR) of both materials was obtained by performing resistance measurements (2-wire) while sweeping the temperature up and down in the range 20 °C–90 °C while keeping the test devices inside a climate chamber (Weiss WKL34) with constant relative humidity ($RH = 50 \pm 2\%$). Then, to assess the effect of the RH over a wide range, the temperature was kept constant (40 ± 1 °C) and the RH was varied from 20% to 80% and vice versa (a full RH cycle). To calculate the TCR and humidity sensitivity, the first portion of the cycle was used (sweep up). The resistance variation of the connecting cables and Ni pads due to temperature and RH changes was subtracted in order to isolate the response of the printed materials. Although the test structures were printed on a flexible PET substrate, the PET was attached to a glass slide during electrical characterization in order to suppress any effects due to unintended mechanical bending.

3. Results and discussion

3.1. CNO material characterization

A Raman analysis was carried out to study the physical characteristics of the CNOs (figure 1(a)). Two main peaks appear at 1340 cm^{-1} and 1585 cm^{-1}, corresponding to the D and G band of CBMs, respectively [31, 32]. The D band can be attributed to disorder and atomic defects within the graphitic layers of the CNO structure. The G band represents the vibrations of carbon atoms (in-plane stretching) within the sp^2 graphitic layers [33–35]. The D-band to G-band intensity ratio gives an estimation of the average defect density. The value of 0.92 found for the CNOs is in line with previously reported values [36]. The purity of the CNOs was evaluated by XPS. The high-resolution C1s spectrum (figure 1(b)) shows a well-defined peak that can be deconvoluted into different components typical of graphitic material: the intense peak at 284.4 eV corresponds to sp^2 graphitic carbon, while the peak at 287.5 eV can be attributed to oxidized carbon groups [37, 38]. The latter could form in correspondence to defects or vacancies in the carbon lattice, in agreement with Raman analysis. The textural properties of the CNOs were analysed by N$_2$ adsorption/desorption isotherms (figure 1(c), (d)), which allow to estimate the specific surface area and pore size distribution. Figure 1(c) shows the adsorption/desorption isotherms plots of CNO obtained at 150 °C. The plot exhibits a type IV isotherm with a hysteresis loop, typical
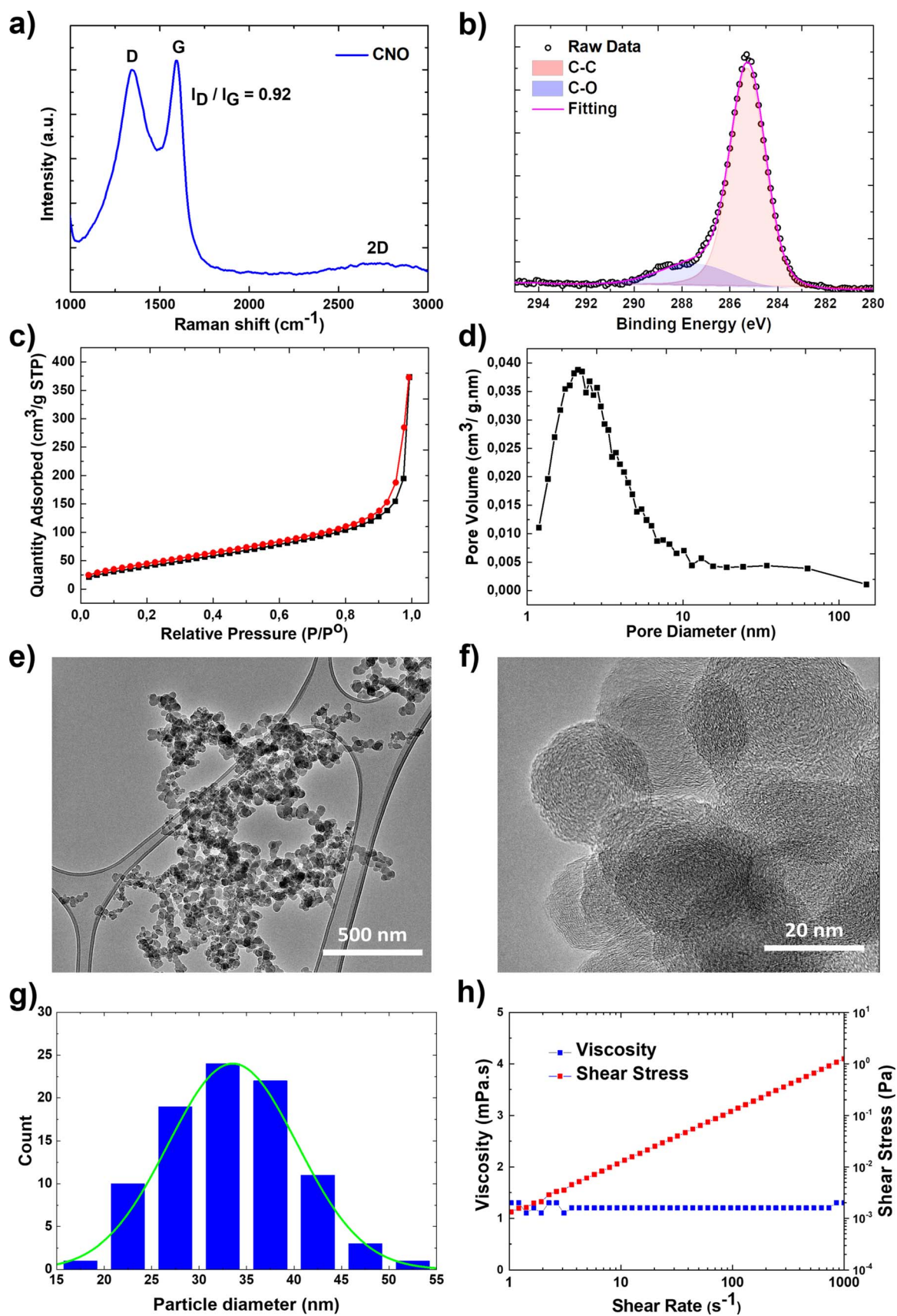
Figure 1. CNO material and ink characterization. (a) Raman spectrum of the prepared CNO. (b) High-resolution C1s XPS spectrum. (c) N_2 adsorption (black line) and desorption (red line) isotherms. (d) Pore size distribution of as-prepared OLC. (e) TEM image of as-prepared CNOs, agglomerated on the TEM grid. (f) High-resolution TEM image of individual CNOs, showing their inner structure. (g) CNO size distribution histogram obtained from TEM image analysis. (h) Viscosity/flow curve of the 6 mg ml^{-1} ethanol-based ink.

Figure 2. Optimization of the jetting parameters. Effect of the first part of the driving pulse (Δt_1) on drop volume and velocity. (a) Ag-NP ink. (b) CNO ink. The green regions identify conditions without satellite drops.

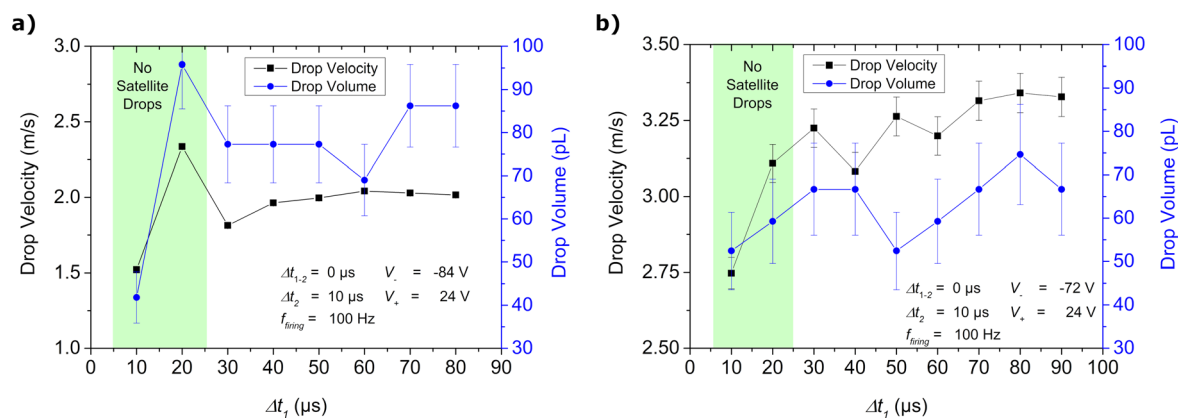of mesoporous materials, due to capillary condensation in the meso-to-microporous structure of the material. The hysteresis loop is a mixed type of H1 and H3—the former is associated with uniform meso-pores, while the latter is related to the presence of non-rigid aggregates of plate-like particles [39–41]. The specific surface area, S_{BET} (measured using BET) of the CNOs is 160 m^2 g^{-1}, which is higher than previously reported [38, 42]. Figure 1(d) shows the pore size distribution obtained from the N_2 desorption branch (using the BJH method), indicating that the CNOs contain both meso- and micro-pores with diameter ranging from 1.7 to 40 nm (with a maximum at 2.2 nm and the majority falling within 10 nm). The total pore volume at $P/P_0 = 0.95$ is 0.24 cm^3 g^{-1}. The morphology of the CNOs was confirmed by TEM imaging, which shows that the particles have a spherical shape with a tight size distribution (figure 1(e)). The inner structure of individual CNOs appears composed of several concentric graphite layers (figure 1(f)), as expected [43, 44]. A TEM statistical analysis of the CNO size was conducted by measuring the diameter of more than 100 individual particles (figure 1(g)). The diameter histogram was fitted with a Gaussian distribution (green line), evidencing an average value of ∼33 nm. The as-synthesized CNOs are hydrophobic in nature, thus the preparation of aqueous inks needs further post-processing in order to get stable dispersions [45]. Consequently, ethanol was used as a solvent in this work. The rheology of the CNO ink in ethanol was investigated by measuring the dynamic viscosity as a function of the shear rate, at 25 °C. Figure 1(h) shows the measured viscosity curve for the ink, highlighting a pseudo-Newtonian behavior with an average dynamic viscosity of 1.2 mPa.s for a broad range of shear rates (1–1000 s^{-1}), just slightly higher than what is reported for pure ethanol [46], due to the low concentration of CNO particles in the solvent.

3.2. Optimization of jetting and printing parameters

Prior to printing, the drop generation conditions were optimized in order to minimize the drop size and avoid satellite drops. The length of the first and second parts of the bipolar excitation pulse, the interval, and the amplitudes of the

negative and positive swings of the pulse were swept and the effects on the drop velocity and drop volume were assessed. Figure 2 illustrates the effect of Δt_1 (everything else constant) for the Ag-NP ink and the CNO ink and shows that both the drop volume and velocity can be customized. Modifying the amplitudes of both portions of the pulse (V_+ and V_-) also allows to modulate the drop velocity and volume to some extent. The minimum drop volumes and velocities were achieved when using the lowest Δt_1 and Δt_2, with $\Delta t_{1-2} = 0$, while using only the minimum possible voltages. The optimized droplet volume (and velocity) was 42 pl (1.5 m s^{-1}) for the Ag-NP ink and 52 pl (2.7 m s^{-1}) for the CNO ink. However, not all conditions tested allowed the jetting of a single drop and often satellite drops appeared. The occurrence of satellite drops can be problematic if the satellite does not merge with the main drop or if it has a different trajectory, which results in the printing of unwanted artifacts that were not present in the original design. Thus, in this case, satellite drops were avoided by selecting the appropriate conditions, as summarized in table 1. The use of the smallest drop volumes guaranteed an optimum resolution for the current nozzle size. The ink backpressure was adjusted to prevent excessive nozzle wetting. For the case of the Ag-NP ink, a slightly negative backpressure of −2 to −4 cm H_2O (roughly −196 to −392 Pa) prevented the flooding of the nozzle and allowed reliable long-term printing. The CNO ink, with a higher solvent volatility (ethanol) and lower surface tension (∼22 mN m^{-1} [47]), was kept approximately at atmospheric pressure (within the range ±98 Pa).

For flexible printed electronics, feature continuity and uniformity are of utmost importance. Thus, after optimizing the jetting parameters for reliability and to obtain the smallest possible drop size, the effects of the printing speed on line continuity and contour were studied. For this purpose, the inkjet head firing frequency was kept at 10 Hz and various stage speeds were tested. The firing rate is unusually low in this study (compared to industry standards) due to the low top speed of the precision stage used for scanning. The firing rate and scan speed can be scaled up according to the specific equipment used. In our case, jetting was reliable even above 500 Hz. For the Ag-NP lines, 1.0 mm s^{-1} provided the best

Table 1. Jetting parameters for minimum drop size and no satellite drops. The single-pass line printing and ink curing conditions are also listed.

	Fluid/ink	DI water	Glycerol solution	Ag-NP	CNO
Jetting parameters	Viscosity (mPa.s)	1	6	6.9 [49]	1.2
	Solvent	Water	Water	Water	Ethanol
	Density (g.cm^{-3})	1	1.13	1.83 [49]	~0.79
	Surface (mN.m^{-1})	71.68	68	29 [49]	~22
	Average particle size (nm)	—	—	37 [49]	33.5
	Backpressure (cm H$_2$O)	0	0	−4	0
	Firing frequency (Hz)	100	100	100	100
	Type of driving pulse	Bipolar	Bipolar	Bipolar	Bipolar
	V_+ (V)	24	24	24	24
	V_- (V)	−24	−84	−84	−72
	Δt_1 (μs)	100	10	10	10
	Δt_{1-2} (μs)	0	0	0	0
	Δt_2 (μs)	10	10	10	10
	Drop volume (pL)	27.6 ± 4.6	41.8 ± 5.9	41.8 ± 5.4	52.4 ± 8.9
	Drop velocity (m.s^{-1})	0.808 ± 0.010	1.618 ± 0.013	1.520 ± 0.013	2.748 ± 0.052
	Satellite drops? (Y/N)	N	N	N	N
Line printing	Firing frequency (Hz)	—	—	10	10
	Stage speed (mm.s^{-1})	—	—	1.0	0.9
	Average linewidth on PET (μm)	—	—	112 ± 16	224 ± 3
	Curing temperature (°C)	—	—	120	120
	Curing time (min)	—	—	60	5

resolution (line width of ~112 μm) and line continuity, with good uniformity and coalescence between drops. For the CNO ink, a speed of 0.9 mm s^{-1} resulted in a good superposition of drops and a consistent thickness along the center of the line. For the CNO ink, the line width was ~224 μm. Optical microscopy images of line printing with various stage speeds (constant firing rate) are in figure S3.

For many devices requiring 1–10 μm thick layers while preserving spatial resolution, multi-pass printing is the obvious solution. In this case, if the ink solvent does not evaporate during the printing scan time (time of the head traveling from one edge of the pattern to the other), inter-layer curing must be implemented in between each printing pass, or a heated substrate must be used. Here, the effects of multi-pass printing without inter-layer curing were tested by printing lines (figure S4) using the Ag-NP ink (up to 20 passes) and the novel CNO ink (up to 200 passes) with the optimum conditions obtained in the previous section (table 1). After the multi-pass printing, the inks were cured by heating the substrates at 120 °C for 60 min (Ag-NP ink) or 5 min (CNO ink). Then, optical microscopy, stylus profilometry and SEM inspection were performed on the printed lines. The layer thickness, linewidth and cross-sectional area for the multi-pass printing with both inks are evaluated using the thickness profiles (shown in figure S5), and are summarized in table 2, which also contains the results of the electrical characterization of the materials.

Given the aqueous-based nature of the commercial Ag-NP ink used in this study, the IJP of a line for over two passes results in the increase of the liquid volume and the spread of the ink over the substrate, increasing the width of the line and resulting in degraded resolution (see figures S4 and S5). The

thickness of a single-pass printed layer with Ag-NP ink is 0.346 ± 0.019 μm, while for two-pass the thickness doubles (0.798 ± 0.040 μm) without linewidth degradation. The previous conclusions are substrate-dependent, as the actual resolution depends on the interaction of the ink with the substrate (as assessed by the contact angle, for example) and substrate roughness. In the cases of the single-pass and double-pass IJP of Ag-NP ink, the use of a more hydrophobic substrate might have resulted in slightly better resolution. Here, thermal curing was performed at the end of the printing process, but alternatives such as photonic flash annealing, laser sintering, hot air annealing and others exist [48].

When printing with the CNO ink, fast solvent evaporation was observed (<1 s), thus it is possible to perform multi-pass printing without degradation of the resolution (the linewidth is constant at ~220 μm). In this study, up to 200 passes were performed (2.7 μm-thick line), but even a greater thickness could have been deposited. Optical microscopy and profilometry results are in figures S4 and S5. The inkjet drop volume for the CNO ink is only ~24% larger than that of the Ag-NP ink (52 pl versus 42 pl), but the printed linewidth obtained with the CNO ink is double of that obtained with the Ag-NP ink, due to the different wetting of the substrate by the solvent. The contact angles (θ) of both inks on PET were measured using a standard technique (drops of 5 μL), for comparison purposes. The water-based Ag-NP ink exhibited θ = 31.4 ± 3.9°, higher than that of the ethanol-based CNO ink (θ = 13.9 ± 3.9°). Despite the fast evaporation of the droplets of the CNO ink upon contact with the substrate, the lower surface tension of the CNO ink is responsible for the spreading of the liquid on substrate (as evidenced by the lower contact angle), resulting in larger minimum feature size

Table 2. Multi pass printing with Ag-NP and CNO inks, without inter-layer curing. Line thickness, width and cross-sectional area. Material resistivity, TCR and humidity sensitivity after curing.

	Number of passes (n)	Line thickness (μm)	Line width (μm)	Cross-sectional Area (μm^2)	Volume resistivity (Ω m)	TCR, α (°C^{-1})	Humidity sensitivity, β (RH$_\%^{-1}$)
Ag-NP	1	0.346 ± 0.019	112 ± 16	35.7	$2.67 \times 10^{-4} \pm 3.4 \times 10^{-5}$	$3.749 \times 10^{-2} \pm 9.9 \times 10^{-4}$	$1.56 \times 10^{-3} \pm 1.29 \times 10^{-4}$
	2	0.798 ± 0.040	117 ± 19	78.5			
	5	1.431 ± 0.121	166 ± 83	242.8			
	20	2.515 ± 0.262	342 ± 146	653.9			
CNO	5	0.072 ± 0.031	235 ± 12	17.02	593 ± 79	$-4.350 \times 10^{-2} \pm 2.54 \times 10^{-3}$	$-1.29 \times 10^{-2} \pm 1.03 \times 10^{-3}$
	10	0.176 ± 0.041	256 ± 6	35.76			
	25	0.341 ± 0.080	239 ± 8	69.04			
	50	0.719 ± 0.127	244 ± 11	124.89			
	100	1.488 ± 0.235	215 ± 7	211.04			
	200	2.730 ± 0.325	244 ± 5	347.46			

Figure 3. Demonstration of complex pattern printing: macro photograph of the institutional logo (INL), printed with the CNO ink (25 printing passes).
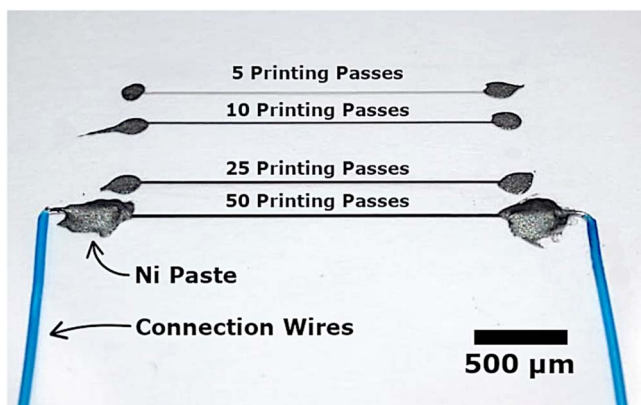

Figure 4. Picture of CNO printed lines, using multi-pass printing, and 2-wire electrical connection for environmental sensitivity characterization.

and linewidth. For better spatial resolution, other solvents or substrate treatments could be considered. For reference, the contact angles of the pure solvents (on PET) were $\theta = 54.5 \pm 4.0°$ for water, and $\theta = 12.9 \pm 2.8°$ for ethanol. Due to the low concentration of CNO in suspension, the contact angle of pure ethanol is identical to that of the CNO ink (within the error of the measurement). Multi-pass test lines with identical thickness ($\sim$700 nm), made of Ag-NP (2-pass printing) and CNO (50-pass printing) were inspected by SEM to investigate the structure of the material after printing and curing. In the Ag-NP print (figure S6(a)), the NPs clustered in grains with size in the 100–400 nm range (with the exception of a few particles as big as a few μm). The CNO print (figure S6(b)) also shows agglomerates with CNO clusters, most likely related to the fast solvent evaporation during the printing process. To demonstrate the production of complex patterns by inkjet, the logo of the institution was printed on a PET substrate (figure 3).

3.3. Electrical characterization for sensor applications

3.3.1. Room temperature electrical resistivity. To perform electrical resistance measurements, test lines with a length of 2 cm and with similar thickness were printed on polymer substrates (PET) with the Ag-NP and CNO inks. Figure 4 contains an example of CNO test lines printed on a PET substrate. Taking the experimental electrical resistance (R),

the length of the test structures (L), and the corresponding cross-sectional area A (obtained by integrating the line profiles), the electrical resistivity (ρ) was calculated using

$$\rho = \frac{A}{L}R. \tag{1}$$

In the case of the Ag-NP, the resistivity was $\rho_{\text{Ag-NP}} = 2.67 \times 10^{-4} \pm 3.4 \times 10^{-5}$ Ω.m, comparable to the values specified in the datasheet of the supplier [49]. For CNO, the resistivity was $\rho_{\text{CNO}} = 593 \pm 79$ Ω.m. In the literature it possible to find just a few reports of the electrical resistivity of CNOs. When addressing single CNO structures, with conductance measurements performed using a scanning tunneling microscope, it was found that the conductance of CNOs modified with $(-\text{CONH-(CH}_2)_2\text{-SH})$ chains is 1.4 μS and the authors estimated a conductance of $\sim$71.8 μS for unmodified CNOs [50]. For CNOs made by annealing nanodiamonds at temperature higher than 1600 K, the resistivity values are in the range 20–50 Ω.m (measured at 300 K) [51]. The resistivity values obtained experimentally in our study are one order of magnitude larger than the reported in the previous reference, which can be due to printed material porosity, CNO surface chemical terminations and sample size dispersion.

Understanding and modelling the electrical conductivity of a powder sample (such as CNO) is not trivial and such topic has been explored elsewhere in the literature [52–57]. The total resistance of a powder-like structure depends on the individual resistance of each particle and the contacts between them. The contact resistance originates from tunneling and constriction resistance due to the small contact area among particles [53]. Often, the real geometry of the contacts is unknown due to particle roughness, complicating the modelling. Usually, when measuring the conductivity of a powder, the grains are mechanically pressed in order to ensure the electrical contact, but here the printed structures were characterized without any applied pressure and in a flat position. The electrical conductivity (σ_E) of powder aggregates has been reported to depend on the powder porosity [55, 56]:

$$\sigma_E = \sigma_0(1 - \Theta/\Theta_M)^u, \tag{2}$$

with

$$u = 1 + (1 - \Theta_M)^{4/5}, \tag{3}$$

where σ_0 is the electrical conductivity of the fully dense material, Θ is the actual powder porosity and Θ_M is the tap porosity (the porosity obtained after the powder sample has been vibrated). Immediately after tapping, $\Theta = \Theta_M$, and $\sigma_E \sim 0$ because the particle contacts are points. By applying pressure to the powder and increasing compaction, Θ decreases relative to Θ_M, thus σ_E increases. Equations (2) and (3) are applicable to aggregates of non-oxide particles as well as powder-sintered compacts, and show that by decreasing the porosity, the electrical conductivity is enhanced [56]. Thus, this phenomenon also points towards the possibility of performing pressure or force sensing using CNOs, as an applied force would change the porosity and

modulate the electrical resistance of the sensor. Carbon black, similar to CNOs in the sense that are also composed of nano-sized particles, can exhibit electrical resistivity in a wide range of values (from ~1 to ~1000 Ω.m) depending on the synthesis methods, and it was found that the electrical conductivity is degraded by the increasing concentration of oxygen, sulphur, polyaromatic or aliphatic groups at the surface [52]. As a reference for comparison, commercial carbon black NP inks (water-based) have resistivity in the range 50–80 Ω.m after curing at $100\,°C$–$140\,°C$ [19]. In the case of CNOs, the occurrence of different chemical groups at the surface can change the overall printed material resistivity as it modifies the contact resistance between particles. As discussed in section 3.1, signs of oxidized carbon were identified in the XPS spectrum—this oxidation is at or close to the surface, and is a plausible explanation for the high resistivity of the printed material, as this oxidation increases the point contact resistance. Unlike metal NPs, CNOs cannot be annealed to improve the electrical conductivity, so the only possibilities are to control and minimize surface contaminants, or to reduce the inter-contact resistance of CNOs. The latter objective could be met by reducing the CNOs′ porosity, by adding particles of different sizes or polymers to the ink formulation.

3.3.2. Temperature coefficient of resistance. The next steps were to assess the temperature and *RH* effects on the electrical resistance of printed structures made of both CNO and Ag-NP materials. Here, a 2-wire configuration was used for the measurement, thus the resistance of the Ni pads and electrical connections was subtracted using a control structure with identical pad geometry and connection lengths. The electrical resistance of the test structures was measured as a function of the temperature, as represented in figure 5(a). The temperature was swept up and down in the range $20\,°C$–$90\,°C$ (at constant *RH*), as plotted in figure 5(b). Assuming a constant temperature coefficient of resistance (α), the variation of resistance (dR), due to an infinitesimal temperature variation (dT) can be written as:

$$\frac{dR}{dT} = \alpha\,R, \tag{4}$$

which can be integrated as:

$$\int_{R_0}^{R} \frac{1}{R}dR = \int_{T_0}^{T} \alpha\,dT \Leftrightarrow \ln\left(\frac{R}{R_0}\right)$$
$$= \alpha(T - T_0) \Leftrightarrow \frac{R}{R_0} = e^{\alpha(T-T_0)}, \tag{5}$$

where the R_0 is the resistance at a temperature T_0 and R is the resistance at temperature T. Doing a first-order Taylor series approximation of equation (5) around T_0, a linear dependency of the resistance with the temperature is obtained:

$$\frac{R}{R_0} \approx 1 + \alpha\,(T - T_0), \tag{6}$$

which is the expression commonly found for the resistance variation with temperature. Using the experimental data of the

whole temperature range from figure 5(a), an exponential fit (as per equation (5)) was performed, allowing to extract $\alpha_{Ag-NP} = 3.749 \times 10^{-2} \pm 9.9 \times 10^{-4}$ K^{-1} for Ag-NP, and $\alpha_{CNO} = -4.350 \times 10^{-2} \pm 2.54 \times 10^{-3}$ K^{-1} for CNO-printed test structures. Ag-NP test structures exhibited positive TCRs, typical of metals, while CNO test lines were characterized by a negative TCR. In metals, the conductivity is proportional to carrier density, electrical charge and carrier mobility. Metallic resistivity at room temperature originates in the scattering of conduction electrons by phonons (lattice vibrations), resulting in the loss of energy and momentum that the electron had gained from an applied electric field [58]. Other resistivity mechanisms such as electron scattering by impurities, point, line and planar defects are usually of negligible importance. The temperature dependence of the CNO resembles that of graphite, in which the resistivity decreases with temperature in the range ~0–500 K [59]. At room temperature, graphite samples with a variety of mass densities and measured in different orientations exhibit resistivity in the range 2.2–7.7 $\mu\Omega$.m. In graphite (semi-metal, in which the valence and conduction bands overlap), the resistivity decreases with the increase in temperature from ambient to $\sim300\,°C$: this has been linked to a growing carrier density by thermal excitation, but the mechanism should differ from the hopping conductivity typical of semiconductors (which have a band gap) [60]. For temperatures above that range, the resistivity starts increasing with temperature, as a result of the disturbance of carrier motion caused by thermal vibrations of the carbon hexagonal lattice, which would cancel the effect of the carrier density increment initially occurring [60]. When comparing the TCR of our printed materials with other printed temperature sensors in the literature, we observe that our values ($\sim10^{-2}$ K^{-1}) are approximately one order of magnitude higher than previously reported ($\sim10^{-3}$ K^{-1}) [61–63]. In the case of the printed Ag test lines, we postulate that such a high temperature dependency may be due to the low curing temperature used in our work ($120\,°C$ for 60 min), which results in printed structures with more defects and thus less resemblance to the bulk material. A low curing temperature was used to prevent deformation of the PET substrate (glass transition temperature is $\sim75\,°C$ and the melting point is $\sim255\,°C$). One final note is that the absolute value of α (temperature sensitivity) for CNO and Ag-NP is comparable, thus temperature compensation appears as a possible application for CNO. Short CNO sections could be printed in series with Ag conductive lines or sensors in order to easily achieve temperature compensation.

3.3.3. Relative humidity effects. To further explore the applicability of printed CNOs for sensing applications, the resistance of the test lines was measured as a function of the *RH* (sweep up and down), at constant temperature ($40\,°C$), as plotted in figures 5(c), (d). The resistance variation can be written in a similar fashion as in equation (6), but now as a function of the humidity sensitivity (β):

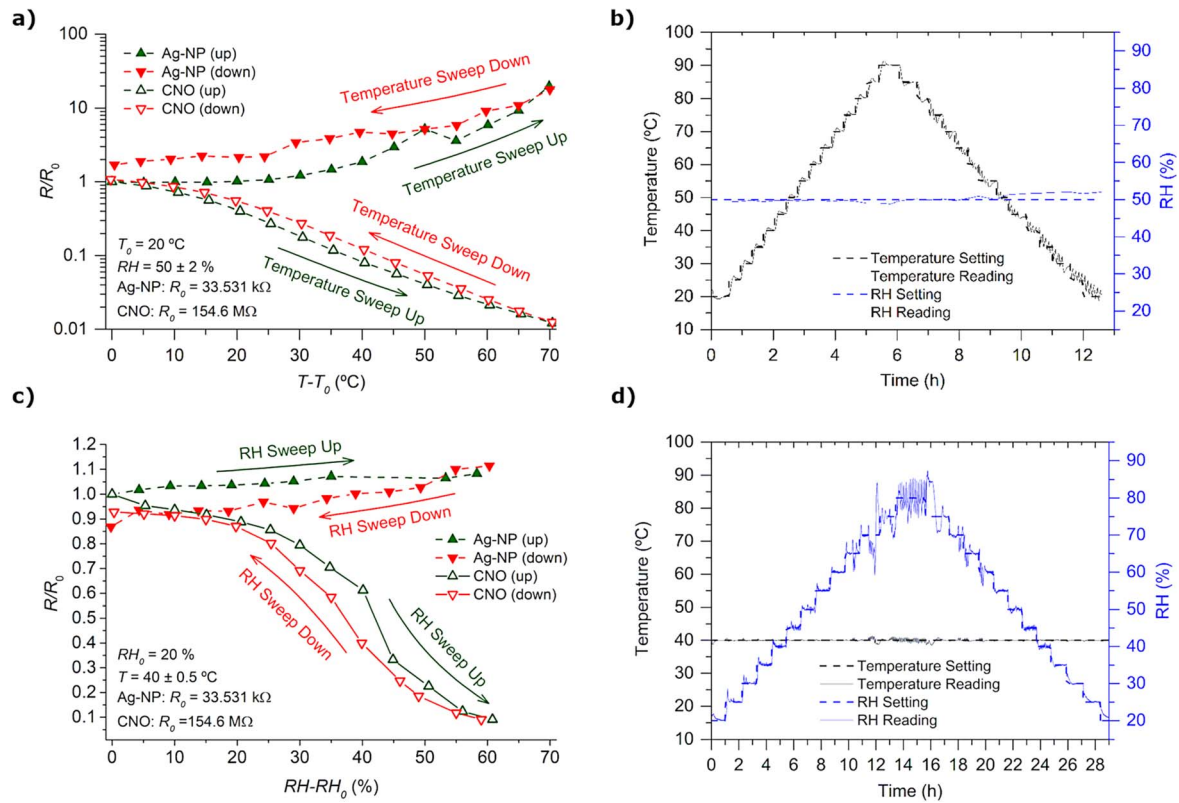$$\frac{R}{R_0} \approx 1 + \beta\,(RH - RH_0), \tag{7}$$

Figure 5. Temperature and *RH* effects on the electrical resistance of printed Ag-NP and CNO test structures. The parameters were swept up and then down to assess for hysteresis effects. (a) Resistance changes as a function of temperature, for a constant *RH*. (b) Typical temperature cycle between 20 °C and 90 °C, with a 5 °C step, measured along time—electrical measurements were made with tolerances of ±0.5 °C and ±2% relative to the settings of temperature and *RH*, respectively. (c) Resistance changes as a function of *RH*, for a constant temperature. (d) Typical *RH* cycle between 20 % and 80%, with a 5 % step, measured along time—electrical measurements were made with tolerances of ±0.5 °C and ±1% relative to the settings of temperature and *RH*, respectively.

where the R_0 is the initial resistance at a relative humidity RH_0 (20%, in our case) and R is the resistance at relative humidity *RH*. The *RH* is specified in percentage points (%), thus the sensitivity β comes in the inverse units, that is, $RH_\%^{-1}$.

The resistance of the Ag-NP-based conductive line exhibited a reduced dependency with the *RH*, with $\beta_{Ag-NP} = 1.56 \times 10^{-3} \pm 1.29 \times 10^{-4}\ RH_\%^{-1}$, thus it varied less than 15% across the tested range of humidity (20%–80%). Further robustness could be achieved by applying an encapsulating dielectric layer on top of the printed Ag-NP features. Contrary to the Ag-NP printed lines, the resistance of the printed CNO lines decreased as much as 91% relative to the initial value, when going from 20% to 80% RH (showing a sigmoidal dependency). The approximate humidity sensitivity of CNO across the whole *RH* range is $\beta_{CNO} = -1.29 \times 10^{-2} \pm 1.03 \times 10^{-3}\ RH_\%^{-1}$, although the resistance change does not follow exactly the linear behavior of equation (7). The sensitivity is lower for *RH* < 40% and there are signs of saturation for *RH* > 70%. The distinct humidity dependency of the Ag-NP and the CNO printed test structures can be explained by the distinct microstructure of both conductive traces and the conduction mechanisms. A trace printed with Ag-NP ink, after curing, is a dense and continuous film (although defective) due to NP coalescence and crystallite growth [64]. However, the CNO-based trace retains the individual NP powder structure, with high porosity and

surface area - due to moisture adsorption, there was an increase of the electrical conductivity of the printed test structures.

Resistive humidity sensors can be fabricated with a variety of materials, such as ceramics [65], semiconductors [66], polymers and composites [67], and CBMs [68]. Depending on the sensor composition, they can exhibit either a positive or a negative resistance dependency with the humidity. For example, some composite humidity sensors made of conductive nanofillers (such as carbon nanotubes) embedded in a hydrophilic polymer matrix exhibit a positive dependence of the resistance with humidity: the polymer matrix swells with increasing humidity, so does the distance between the conductive nanofillers, decreasing the number of electrical connections [67]. Regarding surface electrical conduction, it has been proposed that water molecules present at the surface of silica gel particles can dissociate and provide protons (charge carriers) which are then able to participate in electrical conduction (the resistivity decreases exponentially with the water content) [69]. The protonic conduction is due to the Grotthuss mechanism, through which protons tunnel from one water molecule to the next via hydrogen bonding [70]. Thus, in the case of CNOs, we expect that the decrease of resistance with increasing *RH* is due to ionic conduction at the surface of the CNOs—for confirmation, spectroscopic impedance analysis should be performed in future studies.

The sensor response time and recovery time were not evaluated in our study, because no particular sensor design or optimization was targeted. In the scope of material exploration, we used a long stabilization time before performing the electrical measurement (∼1 h for every set point, as plotted in figure 5(d), and the sweep up data was used for the fits. Table 2 summarizes the results of the geometrical and electrical characterization of the test lines printed with both materials. As discussed before, due to the nanostructure and large specific surface area of CNOs, this material can act as the sensing layer in environmental sensors, such as *RH* sensors, or even in gas sensors, provided that the CNO particles are appropriately functionalized to provide the desired chemical specificity.

4. Conclusions

In this work, the in-depth IJP process development for ethanol-based CNO inks has been reported, showing the workflow for achieving minimum feature size and good line continuity for printed electronics. Such optimization process can be applied to other types of inkjet heads and substrates. The CNO material was synthesized using a low-cost method, which yielded material properties comparable to previously reported CNO samples prepared using other techniques. The use of ethanol as a solvent in the CNO ink allows the multi-pass printing of structures without inter-layer curing. Due to the low CNO concentration, an accurate thickness control is achieved, which can be important in the tuning of the geometry and sensitivity of printed devices and sensors. The printed CNO material exhibited a considerably high electrical resistivity at room temperature ($\sim 10^2$ Ω.m), especially if compared with metallic features such as the ones printed with Ag-NP ink ($\sim 10^{-4}$ Ω.m). Consequently, CNOs should not be considered as an alternative to metal NP inks for the printing of conductive traces. Nevertheless, the CNO resistivity could be lowered by minimizing the concentration of surface contaminants or by combining with other nanomaterials or conductive polymers in the ink formulation (to minimize the inter-particle resistance between individual CNOs).

Considering their properties, CNOs can be regarded as a suitable material for sensing or for temperature compensation applications. Given the elevated sensitivity of the printed CNO material to variations in relative humidity, gas-sensing applications should be further prospected, having in mind the chemical functionalization of CNOs for high specificity, response time, sensor saturation and need for regeneration. The latter application is strongly motivated by the negative TCR of inkjet-printed CNO material, which represents an opposite behavior to metals (such as the printed Ag-NP test devices used for comparison). In terms of process development, the adhesion of CNO to the substrate needs to be optimized, and for flexible applications the reliability should be tested under bending and stretching.

Data availability statement

All data that support the findings of this study are included within the article (and any supplementary files).

ORCID iDs

Rui M R Pinto ● https://orcid.org/0000-0002-8202-9848
Siva Sankar Nemala ● https://orcid.org/0000-0003-2095-3434
Mohammadmahdi Faraji ● https://orcid.org/0000-0001-5270-8631
Giovanni De Bellis ● https://orcid.org/0000-0002-6173-6324
Aritz Retolaza ● https://orcid.org/0000-0002-2916-1794
K B Vinayakumar ● https://orcid.org/0000-0002-6507-9595
Andrea Capasso ● https://orcid.org/0000-0003-0299-6764

References

[1] Khan S, Lorenzelli L and Dahiya R S 2015 Technologies for printing sensors and electronics over large flexible substrates: a review *IEEE Sens. J.* **15** 3164–85
[2] Abbel R *et al* 2014 Industrial-scale inkjet printed electronics manufacturing—production up-scaling from concept tools to a roll-to-roll pilot line *Transl. Mater. Res.* **1** 15002
[3] Corporation N 2023 Metalon® JS-A101A—Nanosilver ink—aqueous dispersions for inkjet printing. [Online] Available: https://novacentrix.com/datasheet/Metalon-JS-A101A-TDS.pdf
[4] Corporation N 2023 Metalon® JS-A211—Nanosilver ink—aqueous dispersion for inkjet printing [Online]. Available: https://novacentrix.com/datasheet/Metalon-JS-A211-TDS.pdf
[5] Pandey A *et al* 2008 Negative temperature coefficient of resistance in a crystalline compound *Europhys. Lett.* **84** 47007
[6] Xiang Z-D, Chen T, Li Z-M and Bian X-C 2009 Negative temperature coefficient of resistivity in lightweight conductive carbon nanotube/polymer composites *Macromol. Mater. Eng.* **294** 91–5

[7] Vishnupriya P P *et al* 2021 Preparation of chip type negative temperature coefficient thermistor *IOP Conf. Ser.: Mater. Sci. Eng.* **1114** 12077

[8] Lu J G *et al* 2006 Structural, optical, and electrical properties of (Zn,Al)O films over a wide range of compositions *J. Appl. Phys.* **100** 73714

[9] Arapov K, Abbel R, de With G and Friedrich H 2014 Inkjet printing of graphene *Faraday Discuss.* **173** 323–36

[10] Capasso A, Del Rio Castillo A E, Sun H, Ansaldo A, Pellegrini V and Bonaccorso F 2015 Ink-jet printing of graphene for flexible electronics: an environmentally-friendly approach *Solid State Commun.* **224** 53–63

[11] Kwon O-S *et al* 2013 Fabrication and characterization of inkjet-printed carbon nanotube electrode patterns on paper *Carbon N. Y.* **58** 116–27

[12] Kang W, Kitamura M and Arakawa Y 2013 High performance inkjet-printed C60 fullerene thin-film transistors: toward a low-cost and reproducible solution process *Org. Electron.* **14** 644–8

[13] Hoth C N, Choulis S A, Schilinsky P and Brabec C J 2007 High photovoltaic performance of inkjet printed polymer: fullerene blends *Adv. Mater.* **19** 3973–8

[14] Withers F *et al* 2014 Heterostructures produced from nanosheet-based inks *Nano Lett.* **14** 3987–92

[15] (John) Zhang C *et al* 2019 Additive-free MXene inks and direct printing of micro-supercapacitors *Nat. Commun.* **10** 1795

[16] Hossain R F and Kaul A B 2020 Inkjet-printed MoS$_2$-based field-effect transistors with graphene and hexagonal boron nitride inks *J. Vac. Sci. Technol.* B **38** 42206

[17] Carey T *et al* 2021 Inkjet printed circuits with 2D semiconductor inks for high-performance electronics *Adv. Electron. Mater.* **7** 2100112

[18] Wen D *et al* 2021 Inkjet printing transparent and conductive mxene (Ti3c2Tx) films: a strategy for flexible energy storage devices *ACS Appl. Mater. Interfaces* **13** 17766–80

[19] Corporation N 2023 Metalon® Jr-700hv—carbon ink—aqueous dispersion for inkjet printing [Online]. Available: https://novacentrix.com/datasheet/Metalon-JR-700HV-TDS.pdf

[20] Pinto R M R, Nemala S S, Faraji M, Capasso A and Vinayakumar K B 2022 Inkjet-printing of carbon nano onions for sensor applications in flexible printed electronics *2022 IEEE Int. Conf. on Flexible and Printable Sensors and Systems (FLEPS)* pp 1–4

[21] Ugarte D 1992 Curling and closure of graphitic networks under electron-beam irradiation *Nature* **359** 707–9

[22] Echegoyen L, Ortiz A, Chaur M N and Palkar A J 2010 Carbon nano onions *Chemistry of Nanocarbons* (United Kingdom: Wiley) pp 463–83

[23] Sano N *et al* 2002 Properties of carbon onions produced by an arc discharge in water *J. Appl. Phys.* **92** 2783–8

[24] Bartelmess J and Giordani S 2014 Carbon nano-onions (multi-layer fullerenes): chemistry and applications *Beilstein J. Nanotechnol.* **5** 1980–98

[25] Mykhailiv O, Zubyk H and Plonska-Brzezinska M E 2017 Carbon nano-onions: unique carbon nanostructures with fascinating properties and their potential applications *Inorg. Chim. Acta* **468** 49–66

[26] Bartkowski M and Giordani S 2020 Supramolecular chemistry of carbon nano-onions *Nanoscale* **12** 9352–8

[27] Giordani S, Camisasca A and Maffeis V 2019 Carbon nano-onions: a valuable class of carbon nanomaterials in biomedicine *Curr. Med. Chem.* **26** 6915–29

[28] Brunauer S, Emmett P H and Teller E 1938 Adsorption of gases in multimolecular layers *J. Am. Chem. Soc.* **60** 309–19

[29] Barrett E P, Joyner L G and Halenda P P 1951 The determination of pore volume and area distributions in porous substances: I. Computations from nitrogen isotherms *J. Am. Chem. Soc.* **73** 373–80

[30] Schneider C A, Rasband W S and Eliceiri K W 2012 NIH Image to ImageJ: 25 years of image analysis *Nat. Methods* **9** 671–5

[31] Ferrari A C and Robertson J 2001 Resonant Raman spectroscopy of disordered, amorphous, and diamondlike carbon *Phys. Rev.* B **64** 75414

[32] Ferrari A C 2007 Raman spectroscopy of graphene and graphite: disorder, electron–phonon coupling, doping and nonadiabatic effects *Solid State Commun.* **143** 47–57

[33] Dresselhaus M S, Jorio A and Saito R 2010 Characterizing graphene, graphite, and carbon nanotubes by raman spectroscopy *Annu. Rev. Condens. Matter Phys.* **1** 89–108

[34] Pimenta M A, Dresselhaus G, Dresselhaus M S, Cancado L G, Jorio A and Saito R 2007 Studying disorder in graphite-based systems by raman spectroscopy *Phys. Chem. Chem. Phys.* **9** 1276–90

[35] Roy D *et al* 2003 Characterisation of carbon nano-onions using raman spectroscopy *Chem. Phys. Lett.* **373** 52–6

[36] Mohapatra D *et al* 2020 Carbon nano-onion-powered optically transparent and economical dye-sensitized solar cells *Nanoscale* **12** 20621–30

[37] Hsiao M-C *et al* 2010 Preparation and properties of a graphene reinforced nanocomposite conducting plate *J. Mater. Chem.* **20** 8496–505

[38] Mohapatra D, Badrayyana S and Parida S 2016 Facile wick-and-oil flame synthesis of high-quality hydrophilic onion-like carbon nanoparticles *Mater. Chem. Phys.* **174** 112–9

[39] Guo F, Creighton M, Chen Y, Hurt R and Külaots I 2014 Porous structures in stacked, crumpled and pillared graphene-based 3D materials *Carbon N. Y.* **66** 476–84

[40] Li J 2022 Porous defective carbon ferrite for adsorption and photocatalysis toward nitrogen compounds in pre-treated biogas slurry *Sci. Rep.* **12** 10789

[41] Thommes M *et al* 2015 Physisorption of gases, with special reference to the evaluation of surface area and pore size distribution (IUPAC Technical Report) *Pure Appl. Chem.* **87** 1051–69

[42] Dhand V, Prasad J S, Rao M V, Bharadwaj S, Anjaneyulu Y and Jain P K 2013 Flame synthesis of carbon nano onions using liquefied petroleum gas without catalyst *Mater. Sci. Eng.* C **33** 758–62

[43] McDonough J K and Gogotsi Y 2013 Carbon onions: synthesis and electrochemical applications *Electrochem. Soc. Interface* **22** 61

[44] Zeiger M, Jäckel N, Mochalin V N and Presser V 2016 Review: carbon onions for electrochemical energy storage *J. Mater. Chem.* A **4** 3172–96

[45] Mohapatra J *et al* 2018 Enzymatic and non-enzymatic electrochemical glucose sensor based on carbon nano-onions *Appl. Surf. Sci.* **442** 332–41

[46] Kaye G W C and Laby T H 1986 *Tables of Physical and Chemical Constants* 15th edn (Harlow: Longman Publishing Group)

[47] Vazquez G, Alvarez E and Navaza J M 1995 Surface tension of alcohol + water from 20 °C to 50 °C *J. Chem. Eng. Data* **40** 611–4

[48] Perelaer J *et al* 2010 Printed electronics: the challenges involved in printing devices, interconnects, and contacts based on inorganic materials *J. Mater. Chem.* **20** 8446–53

[49] Corporation N 2023 Metalon® JS-A221AE—aerosol Ink—aqueous-based silver dispersion [Online]. Available: https://novacentrix.com/datasheet/Metalon-JS-A221AE-TDS.pdf

[50] Sek S, Breczko J, Plonska-Brzezinska M E, Wilczewska A Z and Echegoyen L 2013 STM-based molecular junction of carbon nano-onion *Chem. Phys. Chem* **14** 96–100

[51] Kuznetsov V L, Butenko Y V, Chuvilin A L, Romanenko A I and Okotrub A V 2001 Electrical resistivity

of graphitized ultra-disperse diamond and onion-like carbon *Chem. Phys. Lett.* **336** 397–404

[52] Pantea D, Darmstadt H, Kaliaguine S, Sümmchen L and Roy C 2001 Electrical conductivity of thermal carbon blacks: Influence of surface chemistry *Carbon N. Y.* **39** 1147–58

[53] Celzard A, Marêché J F, Payot F and Furdin G 2002 Electrical conductivity of carbonaceous powders *Carbon N. Y.* **40** 2801–15

[54] Dias R P, Teixeira J A, Mota M G and Yelshin A I 2004 Particulate binary mixtures: dependence of packing porosity on particle size ratio *Ind. Eng. Chem. Res.* **43** 7912–9

[55] Montes J M, Cuevas F G and Cintas J 2008 Porosity effect on the electrical conductivity of sintered powder compacts *Appl. Phys.* A **92** 375–80

[56] Montes J M, Cuevas F G, Cintas J and Urban P 2011 Electrical conductivity of metal powders under pressure *Appl. Phys.* A **105** 935–47

[57] Ren W, Chen Y, Wang Z, Xue S and Zhang X 2016 Electrical contact resistance of coated spherical contacts *IEEE Trans. Electron Devices* **63** 4373–9

[58] Barmak K and Coffey K 2014 *Metallic Films for Electronic, Optical and Magnetic Applications: Structure, Processing and Properties* (Philadelphia: Woodhead Publishing)

[59] Okada M, Ohta N, Yoshimoto O, Tatsumi M and Inagaki M 2017 Review on the high-temperature resistance of graphite in inert atmospheres *Carbon N. Y.* **116** 737–43

[60] Iwashita N, Imagawa H and Nishiumi W 2013 Variation of temperature dependence of electrical resistivity with crystal structure of artificial graphite products *Carbon N. Y.* **61** 602–8

[61] Jäger J, Schwenck A, Walter D, Bülau A, Gläser K and Zimmermann A 2022 Inkjet-printed temperature sensors characterized according to standards *Sensors* **22** 8145

[62] Wang Y-F *et al* 2020 Fully printed PEDOT:PSS-based temperature sensor with high humidity stability for wireless healthcare monitoring *Sci. Rep.* **10** 2467

[63] Bücher T, Huber R, Eschenbaum C, Mertens A, Lemmer U and Amrouch H 2022 Printed temperature sensor array for high-resolution thermal mapping *Sci. Rep.* **12** 14231

[64] Volkman S K, Yin S, Bakhishev T, Puntambekar K, Subramanian V and Toney M F 2011 Mechanistic studies on sintering of silver nanoparticles *Chem. Mater.* **23** 4634–40

[65] Blank T A, Eksperiandova L P and Belikov K N 2016 Recent trends of ceramic humidity sensors development: a review *Sensors Actuators* B **228** 416–42

[66] Kumar A, Gupta G, Bapna K and Shivagan D D 2023 Semiconductor-metal-oxide-based nano-composites for humidity sensing applications *Mater. Res. Bull.* **158** 112053

[67] Park Y-J, Lee S, Kim B, Kim J-H, So J-H and Koo H-J 2020 Impedance study on humidity dependent conductivity of polymer composites with conductive nanofillers *Composites* B **202** 108412

[68] Tulliani J-M, Inserra B and Ziegler D 2019 Carbon-based materials for humidity sensing: a short review *Micromachines* **10** 232

[69] Anderson J H J and Parks G A 1968 Electrical conductivity of silica gel in the presence of adsorbed water *J. Phys. Chem.* **72** 3662–8

[70] Chen Z and Lu C 2005 Humidity sensors: a review of materials and mechanisms *Sensor Lett.* **3** 274–95